MATERIALS SCIENCE

Atomic to nanoscale chemical fluctuations: The catalyst for enhanced thermoelectric performance in high-entropy materials

Jingyi Wang[1]†, Haotian Gao[1]†, Kunpeng Zhao[1,2]*, Hexige Wuliji[3], Binru Zhao[4], Jie Ma[4], Xingyu Chen[5], Jiawei Zhang[5], Yanping Sui[6], Tian-Ran Wei[1,2], Min Zhu[6,7]*, Xun Shi[1,5]*

High-entropy materials have expanded the frontier for discovering uncharted physicochemical properties. The phenomenon of chemical fluctuation is ubiquitous in high-entropy materials, yet its role in the thermoelectric field is often overlooked. Herein, we designed and synthesized a series of $(Mg_{0.94-n}Yb_{0.26}Sr_{0.26}Zn_m)(Mg_nCd_{0.69}Zn_{0.69-m}Na_x)(Sb_{1.74}Ca_{0.26})$ samples characterized by ultrahigh configurational entropy. These samples exhibit a homogeneous single-phase structure at macroscopic and microscopic scales, yet display notable chemical fluctuations at the atomic to nanoscale. These fluctuations, along with the unusual atomic occupations, lead to an exceptionally low lattice thermal conductivity akin to that of amorphous materials. Combining the optimized carrier concentration and well-maintained carrier mobility, we ultimately achieved a high *zT* value of 1.2 at 750 kelvin, outperforming most previously reported AB_2Sb_2-type Zintls. This study underscores that the atomic to nanoscale chemical fluctuations are the crucial catalyst for the enhanced thermoelectric performance in high-entropy materials.

INTRODUCTION

Confronted with the escalating challenges of depleting natural resources and the suboptimal efficiencies of traditional energy conversion systems, the need for more sustainable energy solutions has become increasingly urgent. Thermoelectric (TE) technology, which is capable of efficiently converting waste heat into electrical energy, emerges as a pivotal solution for its various benefits including environmental sustainability, high reliability, and remarkable versatility (*1*–*4*). The energy conversion efficiency of a TE material is primarily measured by the dimensionless figure of merit, where α, σ, κ, and *T* denote the Seebeck coefficient, electrical conductivity, thermal conductivity, and absolute temperature, respectively. Achieving an optimal *zT* value necessitates a delicate balance: a high α to maximize voltage output, a large σ to promote electron transport, and a minimized κ to preserve temperature gradient. Over the past several decades, large strides have been made in the field of TE materials, with considerable efforts directed toward the decoupling of electrical and thermal transports. This has been achieved through a variety of sophisticated strategies, such as energy band shaping (*5*–*7*), phonon softening (*8*, *9*), hierarchical architecture (*10*, *11*), and structural modularization (*12*).

High-entropy engineering has recently emerged as a strategic approach for decoupling the electrical and thermal transport properties (*13*, *14*). Defined by a composition of five or more principal elements (*15*), high-entropy materials exhibit a remarkable degree of structural intricacy that is pivotal to their exceptional physical properties. A range of TE systems, such as $Mg_{2-\delta}$(Si, Ge, Sn, Bi) (*16*), $(Cu/Ag)_2$(S/Se/Te) (*17*–*20*), (Ag/Mn/Ge/Sb)Te (*21*), and (Pb/Sb/Sn)(S/Se/Te) (*22*–*24*), has been identified and demonstrated outstanding TE performance. The profound chemical complexity inherent in high-entropy materials exerts a large impact on the atomic structure and microstructure. On one hand, the high configurational entropy is conducive to the stabilization of single-phase solid solutions (*16*, *24*). On the other hand, the intricate balance of attractive and repulsive interactions among the constituent elements may give rise to deviations from ideal mixing (*25*, *26*), resulting in phenomena such as chemical fluctuation, chemical ordering, and potential phase separation. Chemical fluctuation refers to the local variations or inhomogeneities in chemical compositions within a material, driven by thermodynamic disturbances or local chemical potential differences. These fluctuations can occur at different scales, from atomic to nanoscale and even macroscopic. In contrast, chemical ordering describes the tendency of different types of atoms to occupy specific lattice positions in a structured and rule-based manner, forming either short-range or long-range order as the system minimizes its energy. The chemical ordering and fluctuations are not merely academic curiosities; they can notably influence material properties. For instance, local chemical ordering can alter the electronic structure (*5*, *7*), affecting properties like electrical conductivity and catalytic activity. Similarly, local chemical fluctuation can impede phonon propagation, thereby reducing thermal conductivity (*27*).

Despite the burgeoning interest in high-entropy materials for TE applications, our understanding of how configurational entropy and chemical fluctuations interplay with TE properties remains limited. Particularly, the impact of chemical fluctuations on the transports of

[1]State Key Laboratory of Metal Matrix Composites, School of Materials Science and Engineering, Shanghai Jiao Tong University, Shanghai 200240, China. [2]Wuzhen Laboratory, Tongxiang 314500, China. [3]School of Materials Science and Engineering, Inner Mongolia University of Technology, Hohhot 010051, China. [4]Key Laboratory of Artificial Structures and Quantum Control, School of Physics and Astronomy, Shanghai Jiao Tong University, Shanghai 200240, China. [5]State Key Laboratory of High Performance Ceramics and Superfine Microstructure, Shanghai Institute of Ceramics, Chinese Academy of Sciences, Shanghai 200050, China. [6]State Key Laboratory of Functional Materials for Informatics, Shanghai Institute of Micro-System and Information Technology, Chinese Academy of Sciences, Shanghai 200050, China. [7]School of Integrated Circuits, Shanghai Jiao Tong University, Shanghai 200240, China.
*Corresponding author. Email: zkp.1989@sjtu.edu.cn (K.Z.); minzhu@mail.sim.ac.cn (M.Z.); xshi@mail.sic.ac.cn (X.S.)
†These authors contributed equally to this work.

electrons and phonons is still unclear. This is because traditional microstructural studies have mainly concentrated on dislocations, nanoprecipitates, and grain boundaries, often sidelining the intricate role of chemical fluctuations. In addition, the multiscale nature of chemical fluctuations, spanning from atomic to microscale, complicates the analysis further.

In this work, we delve into a case study in AB_2Sb_2-type Zintl phases, a promising class of TE materials noted for their compositional versatility, environmental sustainability, and electrical tunability (*28*–*31*). The extensive variety of members within AB_2Sb_2 renders it an exemplary platform for probing the chemical intricacies inherent to high-entropy materials and for examining the subsequent implications on TE properties (*32*). Using an array of state-of-the-art characterization techniques, we have elucidated the atomic to nanoscale chemical fluctuations present in AB_2Sb_2-type high-entropy materials (Fig. 1A), which contributes to an exceptionally low lattice thermal conductivity that approaches the theoretical minimum (Fig. 1B). Concurrently, the coherent lattice boundary across disparate nanoregions remains impervious to electron transport, thereby preserving electrical conductivity. As a result, we have attained a peak zT value of 1.2 at 750 K, surpassing most other AB_2Sb_2-type Zintls (Fig. 1C).

RESULTS

Crystal structure and microstructure characterization

AB_2Sb_2-type Zintl phases allow for diverse elemental compositions, where the A site can be occupied by Mg, Yb, Ca, Sr, Eu, or Ba, whereas the B site can be occupied by Mg, Zn, or Cd (*33*–*36*). Capitalizing on this variability, we synthesized a series of AB_2Sb_2-based high-entropy samples with nominal compositions of $[(Mg_{0.25}Yb_{0.25}Ca_{0.25}Sr_{0.25})(Mg_{0.67}Zn_{0.33})_2]_\delta Sb_2$ ($\delta = 1.05$, 1.11, 1.17, and 1.33) and $[(Mg_{0.25}Yb_{0.25}Ca_{0.25}Sr_{0.25})(Mg_{0.33}Zn_{0.33}Cd_{0.33})_2]_{1.17}Na_xSb_2$ ($x = 0$, 0.006, 0.011, 0.013, 0.015, and 0.02), where Na was introduced to tune the carrier concentrations. These samples were initially designed with Mg/Yb/Ca/Sr at the A site and Mg/Zn/Cd at the B site. Despite the large differences in atomic size, electronegativity, and even valence states among the eight constituent elements (see table S1), we successfully achieve a single-phase AB_2Sb_2 structure in such high-entropy compositions (Fig. 2). The calculated configuration entropy is as high as 20 J mol^{-1} K^{-1}, notably surpassing that of all reported TE materials. Maintaining this pure phase necessitates an unusual 17% excess of A/B elements (figs. S1 and S2), in contrast to the typical 1% excess required to compensate for volatilization and/or oxidation observed in $Mg_{3.03}Sb_2$ matrix samples. The energy-dispersive spectroscopy (EDS) analysis verifies that the measured compositions are roughly consistent with the nominal one (table S2), and the relative oxygen content of high-entropy samples is close to the $Mg_{3.03}Sb_2$ matrix (table S3), suggesting that neither volatilization nor oxidation is the cause of the anomalous 17% excess. The specific reasons for this anomaly will be elucidated below.

Chemical fluctuations at nanoscale

At the microscale, all the elements in high-entropy materials exhibit a uniform distribution (Fig. 2B). However, closer investigation

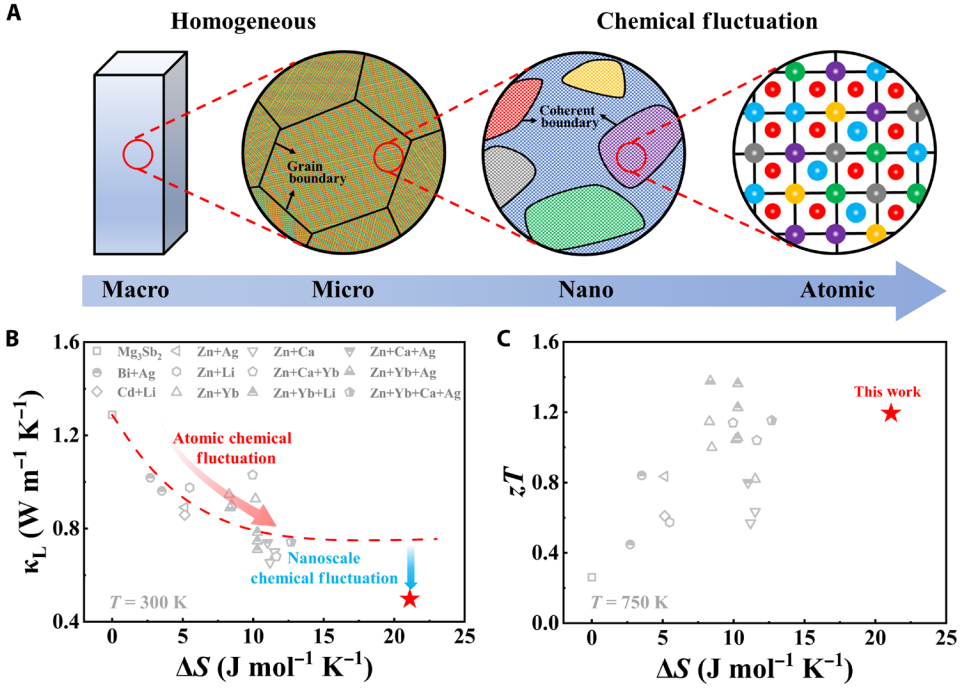

Fig. 1. High-performance Zintl phases TE materials with chemical fluctuations. (**A**) Schematic diagram of atomic to nanoscale chemical fluctuations in high-entropy materials. (**B**) Room temperature lattice thermal conductivity κ_L as a function of configuration entropy ΔS for our high-entropy sample $(Mg_{0.94-n}Yb_{0.26}Sr_{0.26}Zn_m)(Mg_nCd_{0.69}Zn_{0.69-m}Na_x)(Sb_{1.74}Ca_{0.26})$. The red dashed line denotes the theoretical lattice thermal conductivity calculated through the Callaway model (*48*). (**C**) Figure of merit zT at 750 K as a function of configuration entropy ΔS. The reported data of p-type Mg_3Sb_2-based multicomponent samples are included for comparison (*5*, *44*, *49*–*54*).

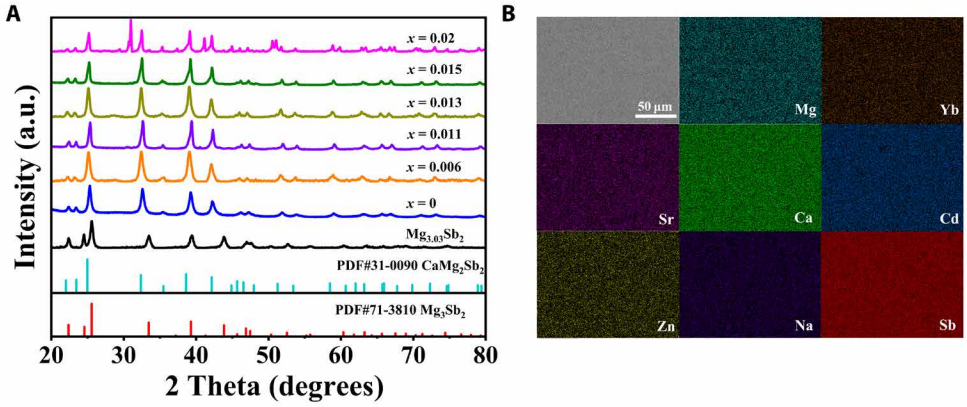

Fig. 2. Crystal structure and microstructure characterization of high-entropy materials. (**A**) Room temperature XRD patterns of samples $[(Mg_{0.25}Yb_{0.25}Ca_{0.25}Sr_{0.25})(Mg_{0.33}Zn_{0.33}Cd_{0.33})_2]_{1.17}Na_xSb_2$ ($x = 0$, 0.006, 0.011, 0.013, 0.015, and 0.02). a.u., arbitrary units. (**B**) Backscattered electron microscopy image and corresponding EDS mapping of the $x = 0.013$ sample.

reveals notable chemical fluctuations at the nano and even atomic levels. Through atom probe tomography (APT) analysis, we have clearly discerned pronounced elemental compositional oscillations at tens of nanometer scale for all constituent elements, including the anionic Sb. For instance, the local maximal concentration of Mg even reaches ~60%, substantially exceeding its nominal concentration (Fig. 3A). Moreover, even after prolonged high-temperature annealing, these marked fluctuations still occur (fig. S3), indicating that such a structure is relatively stable even when sufficient atomic diffusion energy and time are provided. Previous APT results showed no obvious chemical fluctuations in pure Mg_3Sb_2 (*37*, *38*); thus, we believe that the chemical fluctuation phenomena characterized using APT in our study are credible. It should be noted that, in this specimen, the overall elemental concentrations detected by APT deviate from the expected composition as APT focuses on local areas of a few tens of nanometers, which inherently exhibit segregation. To cross-check the chemical fluctuation phenomena, we performed high-angle annular dark field (HAADF) analysis using aberration-corrected scanning transmission electron microscopy (STEM) across different scales and multiple areas. The HAADF image (Fig. 3B) reveals that the high-entropy material consists of dark, gray, and white regions, each spanning several to tens of nanometers. As the intensity of the HAADF image is proportional to the atomic number, this nonuniform contrast indicates an inhomogeneous distribution of elements at the nanoscale. Further EDS mappings directly show that the dark region is enriched with light elements, exemplified by Mg; the white region is enriched with heavier elements, such as Yb and Sr; and the gray region have a higher concentration of Cd and Zn. This observation is confirmed by the quantitative component analysis in the marked regions I, II, and III (Fig. 3C). Notably, despite the compositional variations, the enlarger HADDF image evidences that the different nanoregions remain lattice coherent (Fig. 3D), signifying structural uniformity. This finding is further substantiated by the fast Fourier transform (FFT) analysis, which demonstrates that the three regions display similar diffraction patterns (Fig. 3E). Overall, the chemical fluctuation is observed at the nanoscale while preserving a coherent lattice boundary across different compositions.

Chemical fluctuations at the atomic scale

Further atomic-resolution STEM-EDS mapping provides precise atomic occupation information of various elements within the lattice (Fig. 4). As expected, Yb and Sr elements, with large atomic size and low electronegativity, predominantly occupy the A sites, whereas those with small atomic size and high electronegativity, like Cd, are found exclusively at the B sites. Unexpectedly, Ca atoms were observed to be primarily situated at the Sb sites rather than the A sites typically occupied in $CaMg_2Sb_2$ and $CaZn_2Sb_2$ Zintl phases (*39*), which is highly counterintuitive given the stark differences in properties between Ca and Sb. This peculiar finding, however, well explains the necessity of a 17% excess of cationic elements to synthesize a single-phase alloy as Ca has taken up the anionic site instead of the expected cationic one. We also attempted to explore the atomic structure through synchrotron x-ray atomic pair distribution function (PDF) analysis. The PDF data for the high-entropy sample could be well fitted using the structural model with Ca placing at Sb site (fig. S4), which further confirms this unusual occupancy phenomenon.

To understand the reasons behind this anomalous site occupancy, we performed defect energy calculations. Initially, we constructed a $3 \times 3 \times 2$ supercell of $Mg_{54}Sb_{36}$ and calculated the formation energy for Ca substituting Sb. The calculated formation energy of Ca_{Sb} is as high as 2.26 eV, indicating that Ca is unlikely to occupy the Sb sites in $Mg_{54}Sb_{36}$, which aligns with experimental results from the literature (*39*). Subsequently, we randomly constructed a $3 \times 3 \times 2$ supercell of $(MgYbSr)_6(MgZnCd)_{12}Sb_{36}$ and calculated the formation energy for Ca occupying 36 different Sb sites. We found that, when the surrounding elements of Sb were not solely Mg but were replaced by Yb, Sr, Zn, and Cd, the formation energy of Ca_{Sb} substantially decreased (fig. S5). Notably, the formation energy for certain Sb sites is even below 0.5 eV, substantially lower than the formation energy of Ca_{Sb} (2.26 eV) in the $Mg_{54}Sb_{36}$ matrix. This suggests that changes in the local coordination environment around Sb can drastically reduce the formation energy for foreign element substitution, leading to the observed anomalous site occupancy.

In addition to the anomalous Ca occupancy at Sb sites, we found that Zn does not solely occupy the expected B sites but, like Mg, also occupies A sites. However, the exact concentrations of Zn and Mg at each site remain undetermined. Furthermore, our findings indicate

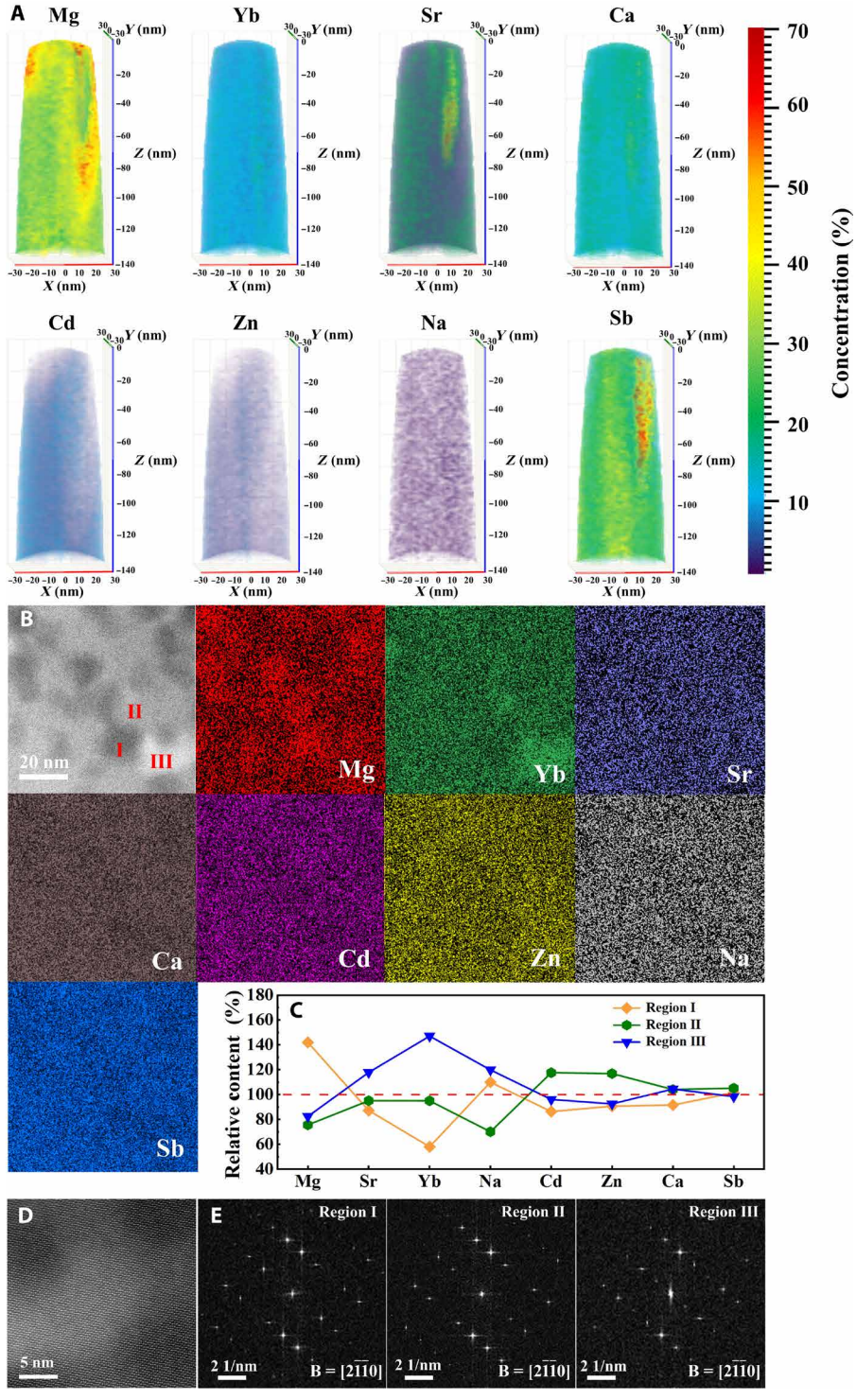

Fig. 3. Chemical fluctuations at the nanoscale of high-entropy materials. (**A**) Three-dimensional reconstruction mappings obtained from the APT technique for the $[(Mg_{0.25}Yb_{0.25}Ca_{0.25}Sr_{0.25})(Mg_{0.33}Zn_{0.33}Cd_{0.33})_2]_{1.17}Na_{0.013}Sb_2$ sample, illustrating the variations in concentrations of the Mg, Yb, Sr, Ca, Cd, Zn, Na, and Sb elements. (**B**) HAADF image and corresponding EDS mapping. (**C**) Relative content of different elements of the dark region I, gray region II, and white region III marked in (B). The red dashed line denotes the relative average content of each element. (**D**) Enlarged HAADF image. (**E**) FFT images of the three different regions in (B).

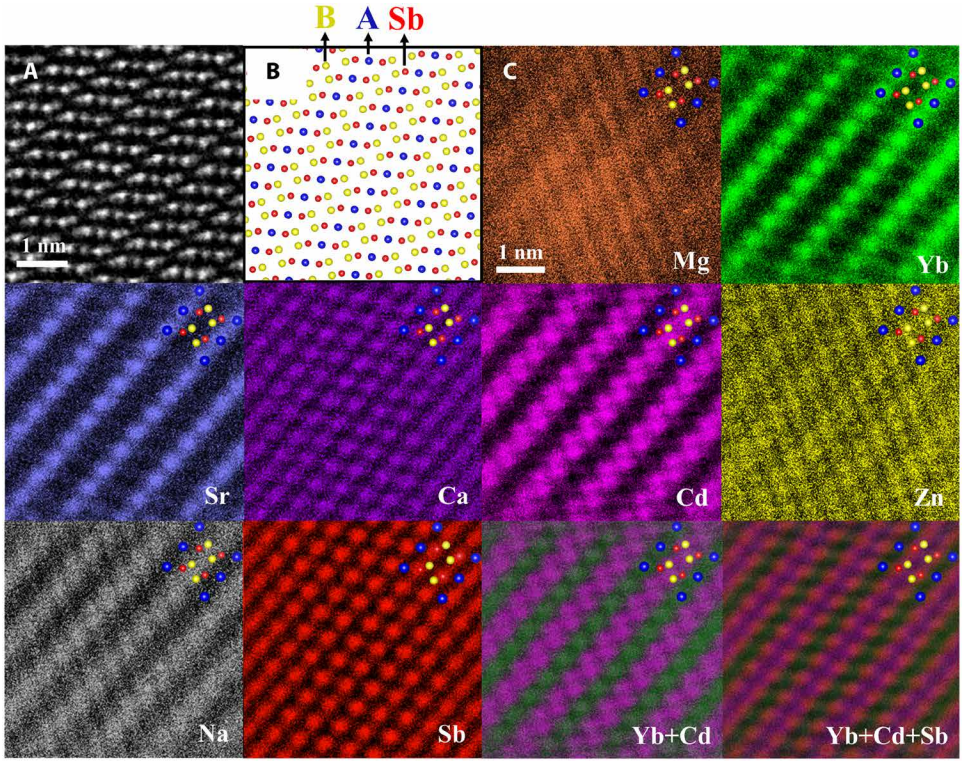

Fig. 4. Chemical fluctuations at the atomic scale in high-entropy materials. (**A**) Atomic-resolution HAADF-STEM images of the high-entropy $(Mg_{0.94-n}Yb_{0.26}Sr_{0.26}Zn_m)(Mg_nCd_{0.69}Zn_{0.69-m}Na_{0.013})(Sb_{1.74}Ca_{0.26})$ sample. (**B**) Corresponding atomic structure model of Zintl phase AB_2Sb_2. (**C**) Atomic-resolution STEM-EDS mappings of various elements. Atomic structure model of AB_2Sb_2 is added in the upper right corner of each figure to calibrate the atomic occupations.

that the elements are not randomly distributed at the atomic scale; instead, there are specific areas with higher concentrations and others with lower concentrations (Fig. 4C). For instance, Yb exhibits stronger contrast in the central-right region of the mapping, indicating a higher content there, whereas its concentration is noticeably lower in the top right and bottom left of the mapping (fig. S6). Further STEM-EDS analysis in a different sample area confirms the presence of these anomalous atomic occupations (fig. S7). Overall, our high-entropy samples exhibit atomic chemical fluctuations, with Yb, Sr, Mg, and Zn disorderedly distributed across the A sites, whereas Cd, Mg, Zn, and Na disorderedly distributed across the B sites. Ca and Sb, on the other hand, share another lattice site in a disordered manner. Consequently, the chemical formula of these high-entropy materials should be revised to $(Mg_{0.94-n}Yb_{0.26}Sr_{0.26}Zn_m)(Mg_nCd_{0.69}Zn_{0.69-m}Na_x)(Sb_{1.74}Ca_{0.26})$, where n and m represent the content of Mg and Zn, respectively, yet to be precisely determined. For consistency, this revised chemical formula will be used in the subsequent discussions.

Thermal transport analysis

The atomic to nanoscale chemical fluctuations in high-entropy materials have a profound impact on both thermal and electrical transports. Figure 5 illustrates the thermal transport properties of high-entropy samples, in comparison with the AB_2Sb_2 matrix samples. The total thermal conductivity κ of the Na-free high-entropy sample is ~0.7 W m^{-1} K^{-1} at 300 K, and it shows a slight increase with the increase in Na content (Fig. 5A), primarily due to the enhanced contribution of electronic thermal conductivity κ_e (fig. S8A). The lattice thermal conductivity κ_L was calculated by subtracting κ_e from the total κ (see calculation details in the Supplementary Materials). The room temperature κ_L of high-entropy samples is only 0.5 to 0.7 W m^{-1} K^{-1}, much lower than all the AB_2Sb_2 matrixes and approach the theoretical minimum estimated by Cahill's model (κ_{min} = 0.52 W m^{-1} K^{-1}) (*40*). It is worth noting that all samples exhibit relative densities greater than 97% (table S4), which suggests that the observed low lattice thermal conductivity is an intrinsic property rather than a result of porosity. With the increase in Na content, there is a slight decrease in lattice thermal conductivity (fig. S8B), which is attributed to the enhanced phonon scattering by point defects. The minor deviations in lattice thermal conductivity for certain samples likely stems from the measurement uncertainties of thermal diffusivity coefficient and the challenges in accurately determining the electronic thermal conductivity. This is underlined by the fact that the Na-doped samples, which show larger electronic conductivities, also show a larger scattering of the determined lattice thermal conductivities. Figure 1B plots the variation of room temperature κ_L against the configurational entropy ΔS for different samples. The solid line represents the prediction based on a widely accepted alloy model that incorporates the influence of atomic fluctuations. It is evident that, as ΔS increases, the κ_L gradually decreases, mainly due to the enhanced phonon scattering caused by atomic-scale lattice distortions. The experimental data for low-entropy samples align with the predicted line, confirming the model's applicability. However, the experimental data for high-entropy samples fall below the predicted values, indicating that the nanoscale chemical fluctuation also has a large impact on suppressing the phonon transport.

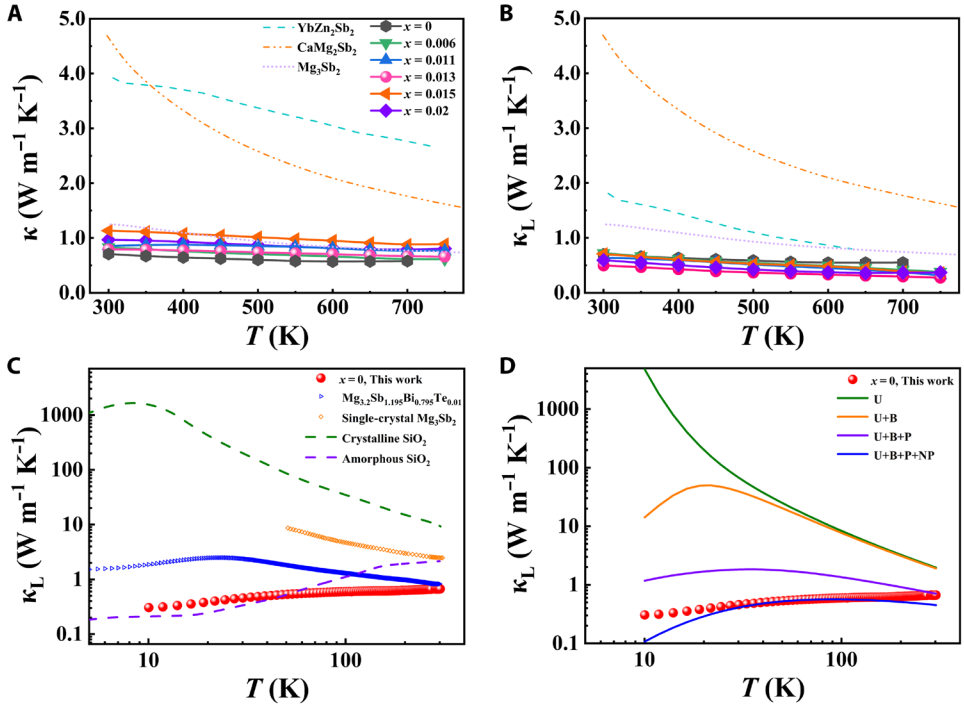

Fig. 5. Thermal properties of high-entropy materials. Temperature dependence of (**A**) total thermal conductivity κ and (**B**) lattice thermal conductivity κ_L for high-entropy $(Mg_{0.94-n}Yb_{0.26}Sr_{0.26}Zn_m)(Mg_nCd_{0.69}Zn_{0.69-m}Na_x)(Sb_{1.74}Ca_{0.26})$, where $x = 0$, 0.006, 0.011, 0.013, 0.015, and 0.02. (**C**) Low-temperature lattice thermal conductivity κ_L as a function of temperature for the $x = 0$ sample. The data of $Mg_{3.2}Sb_{1.195}Bi_{0.795}Te_{0.01}$, single-crystal Mg_3Sb_2 (*55*), crystalline SiO_2 (*56*, *57*), and amorphous SiO_2 (*56*) are included for comparison. (**D**) Contributions from various phonon scattering mechanisms to the lattice thermal conductivity κ_L. U, B, P, and NP denote the phonon-phonon Umklapp process, grain boundary scattering, point defect scattering, and nanoparticle scattering, respectively.

To further delineate the impact of chemical fluctuations on thermal transport, we measured and analyzed the low-temperature (10 to 300 K) thermal conductivity of the high-entropy samples. Unlike conventional crystalline materials that exhibit a pronounced Umklapp peak at around 20 K, the κ_L of our high-entropy samples displays a monotonic increase with temperature (Fig. 5C), a behavior more akin to that of amorphous materials. Moreover, the κ_L of high-entropy samples is obviously lower than those of single crystals and low-to-medium entropy samples, particularly at low temperatures. We used the Debye-Callaway model to fit the low-temperature experimental κ_L (*41*, *42*) (see calculation details in the Supplementary Materials). In this model, atomic chemical fluctuations were treated as point defects, whereas nanoscale chemical fluctuations were considered as nanoparticles. It became evident that only by incorporating the contributions of nanoscale chemical fluctuations could we achieve a satisfactory fit to the experimental data (Fig. 5D). This underscores the indispensable role of nanoscale chemical fluctuations in the suppression of thermal transport, a factor that cannot be overlooked in the design and optimization of high-entropy materials.

Electrical transport analysis

Figure 6 illustrates the electrical transport properties of high-entropy samples, in comparison with the AB_2Sb_2 matrixes. The room temperature carrier mobility μ of our high-entropy samples is around 25 $cm^2\ V^{-1}\ s^{-1}$, which is slightly higher than that of the Mg_3Sb_2 matrix (Fig. 6A). According to the periodic potential theory, the chemical fluctuation on both the atomic scale and nanoscale can disrupt the periodic potential, which typically leads to an increase in carrier scattering. However, despite the presence of chemical fluctuations, the well-defined and coherent atomic lattice can, to some extent, mitigate the scattering effect on charge carriers. Moreover, the band degeneracy and band sharpening effects are also beneficial for the transport of charge carriers, as will be discussed below. With the increase in Na doping content, the carrier concentration p is substantially improved (Fig. 6B), indicating that Na is an effective acceptor in AB_2Sb_2 Zintl phases. The presence of such a high concentration of Ca_{Sb} antisite defects in a material system is also expected to have a large impact on the carrier concentration. However, for high-entropy materials, there are many factors that influence the carrier concentration. The Mg interstitials, Mg vacancies, and even other defects in high-entropy material can all substantially affect the carrier concentration. Furthermore, our x-ray photoelectron spectroscopy (XPS) results (fig. S9) reveal that the valence state of Ca in the high-entropy material deviates from the typical +2 state, complicating the nature of Ca_{Sb} antisite defects. It is possible that these defects act as deep-level defects. The cause of this phenomenon still requires further investigation.

To better elucidate the impact of chemical fluctuations on the electrical transports of high-entropy materials, we analyzed the weighted mobility μ_w relative to the configuration entropy ΔS across different compositions (*43*). μ_w serves as an integrated electrical performance indicator independent of carrier concentrations. The μ_w of our high-entropy samples is ~80 $cm^2\ V^{-1}\ s^{-1}$, outperforming those of the Mg_3Sb_2 matrix and some low-to-medium entropy samples (Fig. 6C). The superior electrical performance could be attributed to the partial band degeneracy or band sharpening within our

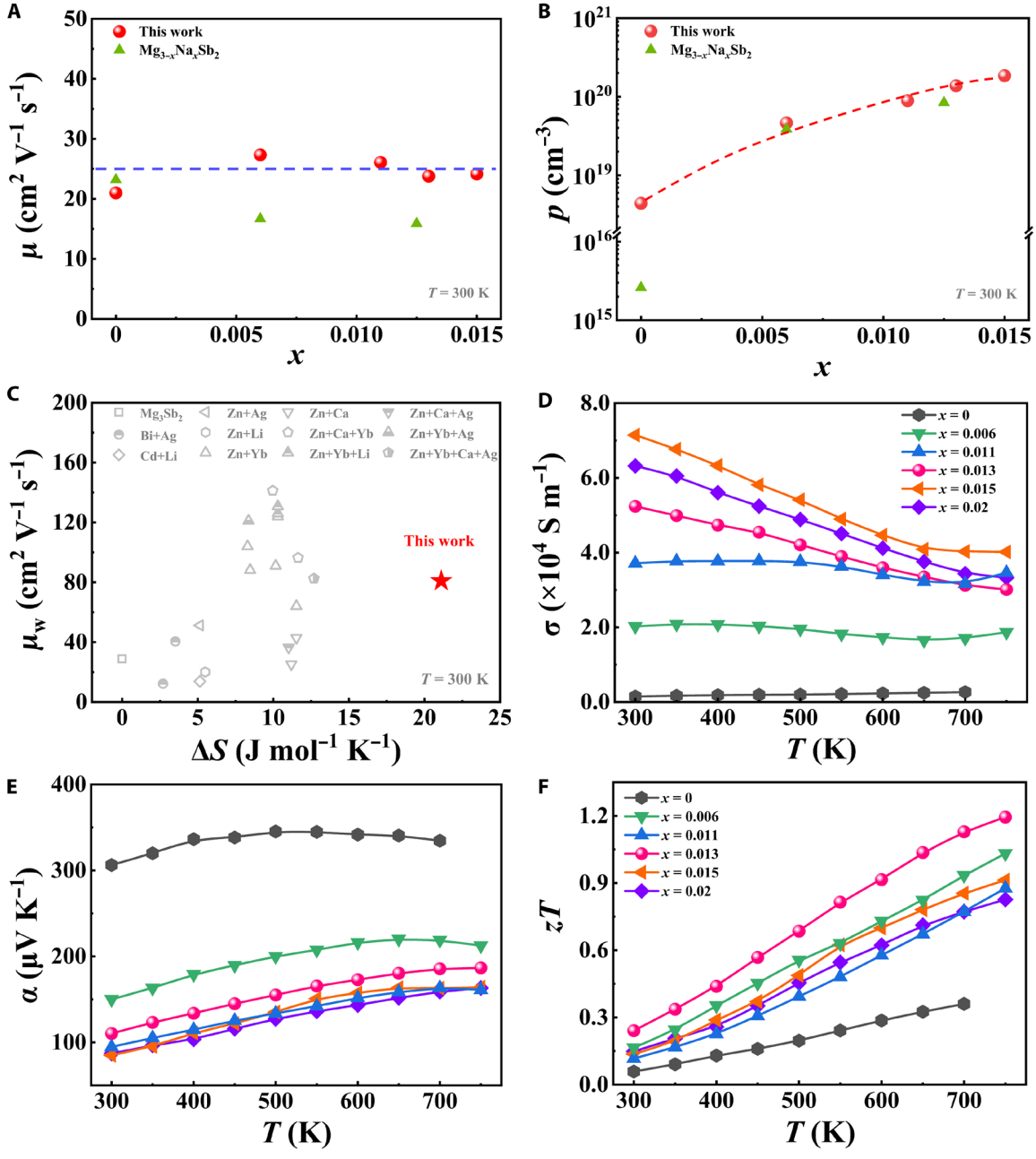

Fig. 6. Electrical properties and figure of merit *zT* of high-entropy materials. (**A**) Carrier mobility μ and (**B**) carrier concentration *p* as functions of Na content *x* for $(Mg_{0.94-n}Yb_{0.26}Sr_{0.26}Zn_m)(Mg_nCd_{0.69}Zn_{0.69-m}Na_x)(Sb_{1.74}Ca_{0.26})$, where *x* = 0, 0.006, 0.01, 0.013, 0.015, and 0.02. Reported data of $Mg_{3-x}Na_xSb_2$ are included for comparison (*58*). (**C**) Weighed mobility μ_w at 300 K as a function of configuration entropy Δ*S*. Reported data of Mg_3Sb_2-based multicomponent samples are included for comparison (*5*, *44*, *49*–*54*). Temperature dependence of (**D**) electric conductivity σ, (**E**) Seebeck coefficient α, and (**F**) figure of merit *zT* in samples $(Mg_{0.94-n}Yb_{0.26}Sr_{0.26}Zn_m)(Mg_nCd_{0.69}Zn_{0.69-m}Na_x)(Sb_{1.74}Ca_{0.26})$ (*x* = 0, 0.006, 0.011, 0.013, 0.015, and 0.02).

high-entropy compositions. From the configuration standpoint, 1 mol of $(Mg_{0.94-n}Yb_{0.26}Sr_{0.26}Zn_m)(Mg_nCd_{0.69}Zn_{0.69-m}Na_x)(Sb_{1.74}Ca_{0.26})$ can be simplistically viewed as a combination of 0.26 mol of $YbCd_2Sb_2$, 0.26 mol of $SrZn_2Sb_2$ and 0.48 mol of Mg_3Sb_2 (*44*). Assuming a linear variation of crystal field splitting energy (Δ) with respect to the components, we calculated Δ for our high-entropy samples as follows: $\Delta = 0.26 \times 0.03\ \text{eV} + 0.26 \times 0.141\ \text{eV} - 0.48 \times 0.40\ \text{eV} = -0.147\ \text{eV}$ (*45*). This result indicates that the positive Δ of $YbCd_2Sb_2$ and $SrZn_2Sb_2$ could partly offset the negative Δ of Mg_3Sb_2. First-principles calculations of the band structure further confirm our inference (fig. S10). The pristine $Mg_{54}Sb_{36}$ has a Δ of ~0.31 eV between its first valence band (VB1) and second valence band (VB2). In contrast, the high-entropy $(MgYbSr)_6(MgZnCd)_{12}Sb_{36}$ exhibits a reduced Δ of only 0.04 eV. The reduction in splitting energy Δ allows the VB2 with small effective mass to participate in electrical transport, thus benefiting carrier mobility. Moreover, we observed a

decrease in the effective mass of both VB1 and VB2, indicative of a band sharpening effect, which also favors carrier transport. Meanwhile, the reduction in lattice parameter ratio a/c in high-entropy materials ($a/c = 0.604$), in contrast to Mg_3Sb_2 ($a/c = 0.631$), is also an indicator of band degeneracy because the energy level of the p_z orbital is more sensitive to Sb-Sb hybridization along the c axis compared with the $p_{x/y}$ orbital (*5*). In Fig. 6C, some reported high-entropy materials exhibit a higher μ_w, likely due to the better band degeneracy effects in these samples. Through adjusting the content of various elements, we believe that the electrical transport performance of our high-entropy samples can be further improved.

Because of the low carrier concentration, the electrical conductivity σ of Na-free samples is very low (~1500 S m^{-1}), whereas the Seebeck coefficient α is very high (reach 300 μV K^{-1}) at room temperature. As the Na content increases, the σ gradually increases, and the α gradually decreases (Fig. 6, D and E). The maximum σ achieved in the $x = 0.015$ sample is about 7×10^4 S m^{-1}, which is two orders of magnitude higher than that of the $x = 0$ sample. It should be noted that the high-entropy samples exhibit excellent thermal stability as the TE performance remain unchanged after rigorous annealing and cycling tests (fig. S11). The relationship between the Seebeck coefficient α and the carrier concentration p can be understood using the well-established Pisarenko plot. As shown in fig. S12, all the data points are distributed around the Pisarenko plot corresponding to effective mass of 1.2 m_e. The data for the $x = 0$ sample fall below this line, whereas the data for the $x = 0.013$ and 0.015 samples lie above it. This indicates that, with increasing Na doping, the effective mass tends to increase. The observed deviations, on one hand, can be partly ascribed to the inherent measurement uncertainties of both carrier concentration and Seebeck coefficient. On the other hand, as Na doping increases, there is a notable rise in hole concentration, which enhances the contribution from the second valence band, consequently leading to an increase in the total effective mass. Thanks to the optimized p and well-maintained μ, the maximum power factor reaches 11 μW cm^{-1} K^{-2} at 650 K for the $x = 0.013$ sample. Consequently, a peak zT value of 1.2 is achieved in the $x = 0.013$ high-entropy material (Fig. 6F), which is superior to most reported AB_2Sb_2-type Zintl phases.

DISCUSSION

Following the high-entropy engineering, we synthesized a series of high-entropy $(Mg_{0.94-n}Yb_{0.26}Sr_{0.26}Zn_m)(Mg_nCd_{0.69}Zn_{0.69-m}Na_x)(Sb_{1.74}Ca_{0.26})$ single-phase materials with homogeneous elemental distribution at the microscopic scale. Using a suite of advanced characterization techniques, we unveiled the precise atomic occupancy of various elements within the high-entropy structure, notably the anomalous positioning of cationic Ca at the anionic Sb site. We found atomic to nanoscale chemical fluctuations that, despite their compositional disparities, maintain a coherent atomic lattice. These chemical fluctuations, coupled with anomalous occupations, can strongly scatter phonons, resulting in an exceptionally low lattice thermal conductivity. After optimizing the carrier concentration, we achieved a remarkable peak zT value of 1.2 at 750 K, ranking among the highest reported values for AB_2Sb_2-type Zintls. This work unveiled the pivotal role of chemical fluctuations in TE transports, charting a promising avenue for the development of innovative high-performance high-entropy materials.

MATERIALS AND METHODS

Sample preparation

A series of AB_2Sb_2-based samples, including $[(Mg_{0.25}Yb_{0.25}Ca_{0.25}Sr_{0.25})(Mg_{0.67}Zn_{0.33})_2]_\delta Sb_2$ (δ = 1.05, 1.11, 1.17, and 1.33), $[(Mg_{0.25}Yb_{0.25}Ca_{0.25}Sr_{0.25})(Mg_{0.33}Zn_{0.33}Cd_{0.33})_2]_{1.17}Na_xSb_2$ ($x = 0$, 0.006, 0.011, 0.013, 0.015, and 0.02), and $Mg_{3.03}Sb_2$ were synthesized using high-energy ball milling methods. High-purity raw materials, including magnesium (99.95%, Aladdin), ytterbium (99.9%, Aladdin), calcium (99.5%, Aladdin), strontium (99.9%, Thermo Fisher Scientific), zinc (99.9%, Zhongsheng Heng'an), cadmium (99.999%, Aladdin), antimony (99.999%, Aladdin), and sodium (99%, Alfa Aesar), were precisely weighed in stoichiometric ratios for the target compositions. In an argon-filled glove box, the weighed raw materials were transferred to stainless steel ball milling jars and milled at 1725 rpm in a Spex-8000D mill for 5 hours, with a midprocess scraping at 2.5 hours to ensure uniform mixing. All operations, including weighing, transferring, and scraping, were performed inside the glove box to maintain an inert atmosphere. After milling, the powders were compacted in a graphite die with a 10-mm diameter and sintered using spark plasma sintering at 903 K for 5 min under a 50-MPa pressure, ensuring the formation of dense bulk samples.

Characterization

Room temperature x-ray diffraction (XRD) analysis was performed using a Bruker D8 Advance diffractometer equipped with Cu K_α radiation (λ = 1.5406 Å). The chemical composition was examined using a field-emission scanning electron microscope (Tescan Mira3, Czech Republic) coupled with an energy-dispersive x-ray spectroscope (Oxford, UK). The XPS characterization was performed using an ESCALAB QXi X-ray Photoelectron Spectrometer Microprobe (Thermo Fisher Scientific, USA). APT analysis was performed in a Cameca Instruments LEAP 5000 XR system. A dc voltage of 2 to 5 kV was applied, with laser pulses at a wavelength of 355 nm and an energy of 30 pJ. A pulse repetition rate was set at 50 kHz, with an average detection rate of 0.2%, and the measurement was performed at a base temperature of 25 K. The APT data were processed using the AP Suite 6.3.2 software from Cameca Instruments. Both the needled-sharped sample and TEM lamella for the APT and TEM analysis, respectively, were prepared through the standard lift-out procedure using a focused ion beam (Helios, Nanolab 600). Atomic-resolution STEM and EDS mapping investigations were conducted on a JEOL JEM-ARM300F microscopy equipped with a dual-probe Cs corrector and an energy-dispersive spectroscope. PDF measurements were performed at the RIKEN BL44B2 beamline at SPring-8, Japan, using a monochromatic x-ray beam with a wavelength of 0.489883(1) Å, which was calibrated through the refinement of the synchrotron diffraction data on a NIST LaB_6 standard. Finely grounded powder with a uniform particle size smaller than 40 μm sealed in 0.2-mm glass capillary was used for the measurements. The diffraction data were appropriately background subtracted and Fourier transformed with a $Q_{max} = 20$ $Å^{-1}$ using PDFgetX3, thus giving the PDF. Instrumental parameters $Q_{damp} = 0.00313$ $Å^{-1}$ and $Q_{broad} = 0.00290$ $Å^{-1}$ were obtained by refining the collected PDF data of the LaB_6 standard in the PDFgui software (*46*). Refinement of the converted PDF data was carried out using the PDFgui software. The sound velocities were measured using an ultrasonic measurement system UMS-100 with shear wave transducers of 5 MHz and longitudinal wave transducers of 10 MHz. Electrical conductivity (σ) and the Seebeck coefficient (S) were assessed using a ZEM-3 system (ULVAC Co. Ltd.) in a helium

environment. Thermal diffusivity (D) was measured using a laser flash method in an argon atmosphere (LFA 457, Netzsch Co. Ltd.). The sample density (ρ) was determined via Archimedes' principle. The specific heat capacity C_p was measured using a differential scanning calorimeter (DSC 404, Netzsch Co. Ltd.) with a heating rate of 5 K/min, and the sapphire was used for correction during the measurement. Total thermal conductivity (κ) was calculated using the formula $\kappa = \rho C_p D$. Carrier concentration (p) and mobility (μ) were derived from the formulas $n = 1/eR_H$ and $\mu = \sigma R_H$, respectively. The Hall coefficient was obtained using the van der Pauw method (M91, Lake Shore Cryotronics Inc., USA) under a magnetic field of 1 T at 300 K. The low-temperature thermal conductivity (10 to 300 K) was measured by a physical property measurement system (PPMS-9, Quantum Design, USA).

Theoretical calculations

All first-principles calculations were performed using the Vienna ab initio simulation package code, using the projector augmented wave method (*47*). The primitive cell of pristine Mg_3Sb_2 was fully relaxed until the total energy and force-convergence criteria were met, with a threshold of 10^{-7} eV and 0.001 eV/Å, respectively. The Perdew-Burke-Ernzerhof functional, within generalized gradient approximation, was applied to handle the electronic exchange and correlation potential. A plane wave energy cutoff of 600 eV was used, and the Brillouin zone was sampled with a 15 × 15 × 7 Γ-centered k-point mesh for structural relaxation. For defect calculations, the atomic coordinates within the supercells are relaxed, maintaining a fixed cell shape and volume, until the total energy and force-convergence criteria reached 10^{-6} eV and 0.01 eV/Å, respectively. A plane wave energy cutoff of 400 eV and a 2 × 2 × 2 Γ-centered k-point mesh were used. Initially, a 3 × 3 × 2 supercell containing 160 atoms was used for defect calculations in the pristine Mg_3Sb_2 system. Subsequently, a 3 × 3 × 2 supercell of $(MgYbSr)_6(MgZnCd)_{12}Sb_{36}$ was randomly constructed for the defect calculations in the high-entropy sample. The crystal structure is illustrated in fig. S5, containing a total of 36 Sb sites. We sequentially substituted a Ca atom for one of the Sb atoms, relaxed the structure, and then calculated the defect formation energies.

Supplementary Materials

This PDF file includes:

Supplementary Text
Figs. S1 to S12
Tables S1 to S6
References

REFERENCES AND NOTES

1. X. L. Shi, J. Zou, Z. G. Chen, Advanced thermoelectric design: From materials and structures to devices. *Chem. Rev.* **120**, 7399–7515 (2020).
2. J. Mao, Z. H. Liu, J. W. Zhou, H. T. Zhu, Q. Zhang, G. Chen, Z. F. Ren, Advances in thermoelectrics. *Adv. Phys.* **67**, 69–147 (2018).
3. G. J. Snyder, E. S. Toberer, Complex thermoelectric materials. *Nat. Mater.* **7**, 105–114 (2008).
4. X. Zhang, L.-D. Zhao, Thermoelectric materials: Energy conversion between heat and electricity. *J. Materiomics* **1**, 92–105 (2015).
5. J. Lei, H. Wuliji, Q. Ren, X. Hao, H. Dong, H. Chen, T.-R. Wei, J. Zhang, P. Qiu, K. Zhao, X. Shi, Exceptional thermoelectric performance in AB_2Sb_2-type Zintl phases through band shaping. *Energ. Environ. Sci.* **17**, 1416–1425 (2024).
6. Y. Pei, H. Wang, G. J. Snyder, Band engineering of thermoelectric materials. *Adv. Mater.* **24**, 6125–6135 (2012).
7. Q. Xu, K. Zhao, H. Huang, S. Wan, Q. Ren, X. Hao, H. Wuliji, J. Lei, T.-R. Wei, X. Shi, Enhancing thermoelectric performance of AB_2Sb_2-type Zintl phase through band shaping and lattice distortion. *Acta Mater.* **274**, 120040 (2024).
8. K. Zhao, Z. Yue, H. Wuliji, H. Chen, T. Deng, J. Lei, P. Qiu, L. Chen, X. Shi, Modeling critical thermoelectric transports driven by band broadening and phonon softening. *Nat. Commun.* **15**, 776 (2024).
9. O. Delaire, K. Marty, M. B. Stone, P. R. C. Kent, M. S. Lucas, D. L. Abernathy, D. Mandrus, B. C. Sales, Phonon softening and metallization of a narrow-gap semiconductor by thermal disorder. *Proc. Natl. Acad. Sci. U.S.A.* **108**, 4725–4730 (2011).
10. K. Biswas, J. He, I. D. Blum, C.-I. Wu, T. P. Hogan, D. N. Seidman, V. P. Dravid, M. G. Kanatzidis, High-performance bulk thermoelectrics with all-scale hierarchical architectures. *Nature* **489**, 414–418 (2012).
11. Y. Pei, G. Tan, D. Feng, L. Zheng, Q. Tan, X. Xie, S. Gong, Y. Chen, J.-F. Li, J. He, M. G. Kanatzidis, L.-D. Zhao, Integrating band structure engineering with all-scale hierarchical structuring for high thermoelectric performance in PbTe system. *Adv. Energy Mater.* **7**, 1601450 (2017).
12. K. Zhao, C. Zhu, M. Zhu, H. Chen, J. Lei, Q. Ren, T.-R. Wei, P. Qiu, F. Xu, L. Chen, J. He, X. Shi, Structural modularization of Cu_2Te leading to high thermoelectric performance near the Mott–Ioffe–Regel limit. *Adv. Mater.* **34**, e2108573 (2022).
13. R. Liu, H. Chen, K. Zhao, Y. Qin, B. Jiang, T. Zhang, G. Sha, X. Shi, C. Uher, W. Zhang, L. Chen, Entropy as a gene-like performance indicator promoting thermoelectric materials. *Adv. Mater.* **29**, 1702712 (2017).
14. B. Jiang, W. Wang, S. Liu, Y. Wang, C. Wang, Y. Chen, L. Xie, M. Huang, J. He, High figure-of-merit and power generation in high-entropy GeTe-based thermoelectrics. *Science* **377**, 208–213 (2022).
15. J.-W. Yeh, S.-K. Chen, S.-J. Lin, J.-Y. Gan, T.-S. Chin, T.-T. Shun, C.-H. Tsau, S.-Y. Chang, Nanostructured high-entropy alloys with multiple principal elements: Novel alloy design concepts and outcomes. *Adv. Eng. Mater.* **6**, 299–303 (2004).
16. H. Gao, K. Zhao, H. Wuliji, M. Zhu, B. Xu, H. Lin, L. Fei, H. Zhang, Z. Zhou, J. Lei, H. Chen, S. Wan, T.-R. Wei, X. Shi, Adaptable sublattice stabilized high-entropy materials with superior thermoelectric performance. *Energ. Environ. Sci.* **16**, 6046–6057 (2023).
17. Z. Zhang, K. Zhao, H. Chen, Q. Ren, Z. Yue, T.-R. Wei, P. Qiu, L. Chen, X. Shi, Entropy engineering induced exceptional thermoelectric and mechanical performances in $Cu_{2-y}Ag_yTe_{1-2x}S_xSe_x$. *Acta Mater.* **224**, 117512 (2022).
18. K. P. Zhao, K. Liu, Z. M. Yue, Y. C. Wang, Q. F. Song, J. Li, M. J. Guan, Q. Xu, P. F. Qiu, H. Zhu, L. D. Chen, X. Shi, Are Cu_2Te-based compounds excellent thermoelectric materials? *Adv. Mater.* **31**, e1903480 (2019).
19. Z. X. Zhang, K. P. Zhao, T. R. Wei, P. F. Qiu, L. D. Chen, X. Shi, Cu_2Se-Based liquid-like thermoelectric materials: Looking back and stepping forward. *Energ. Environ. Sci.* **13**, 3307–3329 (2020).
20. M. Guan, K. Zhao, P. Qiu, D. Ren, X. Shi, L. Chen, Enhanced thermoelectric performance of quaternary $Cu_{2-2x}Ag_{2x}Se_{1-x}S_x$ liquid-like chalcogenides. *ACS Appl. Mater. Interfaces* **11**, 13433–13440 (2019).
21. Z. Ma, T. Xu, W. Li, Y. Cheng, J. Li, D. Zhang, Q. Jiang, Y. Luo, J. Yang, High entropy semiconductor $AgMnGeSbTe_4$ with desirable thermoelectric performance. *Adv. Funct. Mater.* **31**, 2103197 (2021).
22. T. R. Wei, G. J. Tan, X. M. Zhang, C. F. Wu, J. F. Li, V. P. Dravid, G. J. Snyder, M. G. Kanatzidis, Distinct impact of alkali-ion doping on electrical transport properties of thermoelectric p-type polycrystalline SnSe. *J. Am. Chem. Soc.* **138**, 8875–8882 (2016).
23. Z. W. Chen, Z. Z. Jian, W. Li, Y. J. Chang, B. H. Ge, R. Hanus, J. Yang, Y. Chen, M. X. Huang, G. J. Snyder, Y. Z. Pei, Lattice dislocations enhancing thermoelectric PbTe in addition to band convergence. *Adv. Mater.* **29**, 1606768 (2017).
24. B. Jiang, Y. Yu, J. Cui, X. Liu, L. Xie, J. Liao, Q. Zhang, Y. Huang, S. Ning, B. Jia, B. Zhu, S. Bai, L. Chen, S. J. Pennycook, J. He, High-entropy-stabilized chalcogenides with high thermoelectric performance. *Science* **371**, 830–834 (2021).
25. E. P. George, D. Raabe, R. O. Ritchie, High-entropy alloys. *Nat. Rev. Mater.* **4**, 515–534 (2019).
26. N. Oueldna, N. Sabi, H. Aziam, V. Trabadelo, H. B. Youcef, High-entropy materials for thermoelectric applications: Towards performance and reliability. *Mater. Horiz.* **11**, 2323–2354 (2024).
27. W. Wang, S. Liu, Y. Wang, B. Jia, Y. Huang, L. Xie, B. Jiang, J. He, Tailoring local chemical fluctuation of high-entropy structures in thermoelectric materials. *Sci. Adv.* **10**, eadp4372 (2024).
28. S. M. Kauzlarich, S. R. Brown, G. Jeffrey Snyder, Zintl phases for thermoelectric devices. *Dalton Trans.* **21**, 2099–2107 (2007).
29. J. Shuai, J. Mao, S. Song, Q. Zhang, G. Chen, Z. Ren, Recent progress and future challenges on thermoelectric Zintl materials. *Mater. Today Phys.* **1**, 74–95 (2017).
30. J. Zhu, Q. Ren, C. Chen, C. Wang, M. Shu, M. He, C. Zhang, M. D. Le, S. Torri, C.-W. Wang, J. Wang, Z. Cheng, L. Li, G. Wang, Y. Jiang, M. Wu, Z. Qu, X. Tong, Y. Chen, Q. Zhang, J. Ma, Vacancies tailoring lattice anharmonicity of Zintl-type thermoelectrics. *Nat. Commun.* **15**, 2618 (2024).
31. J. Lei, K. Zhao, J. Liao, S. Yang, Z. Zhang, T.-R. Wei, P. Qiu, M. Zhu, L. Chen, X. Shi, Approaching crystal's limit of thermoelectrics by nano-sintering-aid at grain boundaries. *Nat. Commun.* **15**, 6588 (2024).
32. K.-F. Liu, S.-Q. Xia, Recent progresses on thermoelectric Zintl phases: Structures, materials and optimization. *J. Solid State Chem.* **270**, 252–264 (2019).

33. X. Shi, L. Deng, Z. Liang, S. Song, C. Xu, D. Wang, C.-W. Chu, D. J. Singh, Z. Ren, Combined tactics for elevating the thermoelectric performance of $CaMg_2Sb_2$-based p-type materials. *Adv. Electron. Mater.* **8**, 2200742 (2022).
34. J. Sun, D. J. Singh, Thermoelectric properties of AMg_2X_2, AZn_2Sb_2 (A = Ca, Sr, Ba; X = Sb, Bi), and Ba_2ZnX_2 (X = Sb, Bi) Zintl compounds. *J. Mater. Chem. A* **5**, 8499–8509 (2017).
35. Z. Zhang, H. Yao, Q. Wang, W. Xue, Y. Wang, L. Yin, X. Wang, X. Li, C. Chen, J. Sui, X. Lin, Y. Chen, X. Liu, J. Mao, G. Xie, Q. Zhang, Achieving high thermoelectric performance in severely distorted $YbCd_2Sb_2$. *Adv. Funct. Mater.* **32**, 2205215 (2022).
36. C. Chen, W. Xue, S. Li, Z. Zhang, X. Li, X. Wang, Y. Liu, J. Sui, X. Liu, F. Cao, Z. Ren, C.-W. Chu, Y. Wang, Q. Zhang, Zintl-phase Eu_2ZnSb_2: A promising thermoelectric material with ultralow thermal conductivity. *Proc. Natl. Acad. Sci. U.S.A.* **116**, 2831–2836 (2019).
37. J. J. Kuo, Y. Yu, S. D. Kang, O. Cojocaru-Mirédin, M. Wuttig, G. J. Snyder, Mg deficiency in grain boundaries of n-type Mg_3Sb_2 identified by atom probe tomography. *Adv. Mater. Interfaces* **6**, 1900429 (2019).
38. T. Luo, J. J. Kuo, K. J. Griffith, K. Imasato, O. Cojocaru-Mirédin, M. Wuttig, B. Gault, Y. Yu, G. J. Snyder, Nb-mediated grain growth and grain-boundary engineering in Mg_3Sb_2-based thermoelectric materials. *Adv. Funct. Mater.* **31**, 2100258 (2021).
39. M. Wood, U. Aydemir, S. Ohno, G. J. Snyder, Observation of valence band crossing: The thermoelectric properties of $CaZn_2Sb_2$–$CaMg_2Sb_2$ solid solution. *J. Mater. Chem. A* **6**, 9437–9444 (2018).
40. D. G. Cahill, S. K. Watson, R. O. Pohl, Lower limit to the thermal conductivity of disordered crystals. *Phys. Rev. B* **46**, 6131–6140 (1992).
41. J. Callaway, Model for lattice thermal conductivity at low temperatures. *Phys. Rev.* **113**, 1046–1051 (1959).
42. Z. Jin, Y. Xiong, K. Zhao, H. Dong, Q. Ren, H. Huang, X. Qiu, J. Xiao, P. Qiu, L. Chen, X. Shi, Abnormal thermal conduction in argyrodite-type $Ag_9FeS_{6-x}Te_x$ materials. *Mater. Today Phys.* **19**, 100410 (2021).
43. G. J. Snyder, A. H. Snyder, M. Wood, R. Gurunathan, B. H. Snyder, C. Niu, Weighted mobility. *Adv. Mater.* **32**, e2001537 (2020).
44. X. Shi, S. Song, G. Gao, Z. Ren, Global band convergence design for high-performance thermoelectric power generation in Zintls. *Science* **384**, 757–762 (2024).
45. J. Zhang, L. Song, G. K. H. Madsen, K. F. F. Fischer, W. Zhang, X. Shi, B. B. Iversen, Designing high-performance layered thermoelectric materials through orbital engineering. *Nat. Commun.* **7**, 10892 (2016).
46. C. L. Farrow, P. Juhas, J. W. Liu, D. Bryndin, E. S. Božin, J. Bloch, T. Proffen, S. J. L. Billinge, PDFfit2 and PDFgui: Computer programs for studying nanostructure in crystals. *J. Phys. Condens. Matter* **19**, 335219 (2007).
47. P. E. Blöchl, Projector augmented-wave method. *Phys. Rev. B* **50**, 17953–17979 (1994).
48. J. Yang, G. P. Meisner, L. Chen, Strain field fluctuation effects on lattice thermal conductivity of ZrNiSn-based thermoelectric compounds. *Appl. Phys. Lett.* **85**, 1140–1142 (2004).
49. L. Huang, T. Liu, X. Mo, G. Yuan, R. Wang, H. Liu, X. Lei, Q. Zhang, Z. Ren, Thermoelectric performance improvement of p-type Mg_3Sb_2-based materials by Zn and Ag co-doping. *Mater. Today Phys.* **21**, 100564 (2021).
50. L. Wu, Z. Zhou, G. Han, B. Zhang, J. Yu, H. Wang, Y. Chen, X. Lu, G. Wang, X. Zhou, Realizing high thermoelectric performance in p-type $CaZn_2Sb_2$-alloyed Mg_3Sb_2-based materials via band and point defect engineering. *Chem. Eng. J.* **475**, 145988 (2023).
51. Y.-B. Zhang, J.-S. Liang, C. Liu, Q. Zhou, Z. Xu, H.-B. Chen, F.-C. Li, Y. Peng, L. Miao, Enhancing thermoelectric performance in p-type Mg_3Sb_2-based Zintls through optimization of band gap structure and nanostructuring. *J. Mater. Sci. Technol.* **170**, 25–32 (2024).
52. C. Chen, X. Li, S. Li, X. Wang, Z. Zhang, J. Sui, F. Cao, X. Liu, Q. Zhang, Enhanced thermoelectric performance of p-type Mg_3Sb_2 by lithium doping and its tunability in an anionic framework. *J. Mater. Sci.* **53**, 16001–16009 (2018).
53. K.-J. Liu, Z.-W. Zhang, C. Chen, L.-H. Wei, H.-L. He, J. Mao, Q. Zhang, Entropy engineering in $CaZn_2Sb_2$–$YbMg_2Sb_2$ Zintl alloys for enhanced thermoelectric performance. *Rare Metals* **41**, 2998–3004 (2022).
54. X. Tang, B. Zhang, X. Zhang, S. Wang, X. Lu, G. Han, G. Wang, X. Zhou, Enhancing the thermoelectric performance of p-type Mg_3Sb_2 via codoping of Li and Cd. *ACS Appl. Mater. Interfaces* **12**, 8359–8365 (2020).
55. Y. Pan, M. Yao, X. Hong, Y. Zhu, F. Fan, K. Imasato, Y. He, C. Hess, J. Fink, J. Yang, B. Büchner, C. Fu, G. J. Snyder, C. Felser, $Mg_3(Bi,Sb)_2$ single crystals towards high thermoelectric performance. *Energ. Environ. Sci.* **13**, 1717–1724 (2020).
56. D. G. Cahill, R. O. Pohl, Heat flow and lattice vibrations in glasses. *Solid State Commun.* **70**, 927–930 (1989).
57. Y.-G. Yoon, R. Car, D. J. Srolovitz, S. Scandolo, Thermal conductivity of crystalline quartz from classical simulations. *Phys. Rev. B* **70**, 012302 (2004).
58. J. Shuai, Y. Wang, H. S. Kim, Z. Liu, J. Sun, S. Chen, J. Sui, Z. Ren, Thermoelectric properties of Na-doped Zintl compound: $Mg_{3-x}Na_xSb_2$. *Acta Mater.* **93**, 187–193 (2015).
59. R. Simon, Thermoelectric figure of merit of two-band semiconductors. *J. Appl. Phys.* **33**, 1830–1841 (1962).
60. R. A. Swalin, S. A. Rice, Thermodynamics of solids. *Phys. Today* **16**, 72–74 (1963).
61. G. A. Slack, S. Galginaitis, Thermal conductivity and phonon scattering by magnetic impurities in CdTe. *Phys. Rev.* **133**, A253–A268 (1964).
62. P. G. Klemens, The scattering of low-frequency lattice waves by static imperfections. *Proc. Phys. Soc. A* **68**, 1113–1128 (1955).
63. B. Abeles, Lattice thermal conductivity of disordered semiconductor alloys at high temperatures. *Phys. Rev.* **131**, 1906–1911 (1963).
64. S. Chen, J. Wei, Z. Kang, X. Miao, D. An, W. Fan, C. Dun, Enhancement of thermoelectric performance in $Mg_3(Sb,Bi)_2$ through engineered lattice strain and controlled carrier scattering. *Chem. Eng. J.* **490**, 151404 (2024).
65. S.-H. Lo, J. He, K. Biswas, M. G. Kanatzidis, V. P. Dravid, Phonon scattering and thermal conductivity in p-type nanostructured PbTe-BaTe bulk thermoelectric materials. *Adv. Funct. Mater.* **22**, 5175–5184 (2012).

Acknowledgments: We thank the support from the National Natural Science Foundation of China and Science and Technology Commission of Shanghai Municipality. We also thank the synchrotron beamline RIKEN BL44B2 (proposal nos. 2023B1295, 2023B1376, and 2024A1235) at SPring-8 for the beamtime allocation. **Funding:** This work was supported by the National Natural Science Foundation of China (52422214, 92463310, and 52372209), National Outstanding Youth Program (62322411), and Shanghai Pilot Program for Basic Research-Chinese Academy of Science, Shanghai Branch (JCYJ-SHFY-2022-002). **Author contributions:** K.Z. and X.S. designed the study. J.W. and H.G. prepared the samples and carried out the experiments. M.Z. and Y. P. performed the APT and STEM investigation. B.Z. and J.M. measured the low-temperature thermal conductivity. X.C. and J.Z. conducted the atomic PDF experiments. H.W. performed the theoretical calculations. J.W., H.G., K.Z., and T.-R.W. analyzed the experimental data. J.W., H.G., K.Z., and X.S. wrote and edited the manuscript. All authors discussed the results, read the paper, and commented on the text. **Competing interests:** The authors declare that they have no competing interests. **Data and materials availability:** All data needed to evaluate the conclusions in the paper are present in the paper and/or the Supplementary Materials.

Submitted 6 October 2024
Accepted 28 January 2025
Published 28 February 2025
10.1126/sciadv.adt6298